Front. Mater. Sci. 2022, 16(1): 220593
https://doi.org/10.1007/s11706-022-0593-9

RESEARCH ARTICLE

Bimetallic sulfide FeS_2@SnS_2 as high-performance anodes for sodium-ion batteries

Zhenxiao LU (✉), Zixiao ZHAO, Guangyin LIU, Xiaodi LIU, and Renzhi YANG

School of Chemical and Pharmaceutical Engineering, Nanyang Normal University, Nanyang 473061, China

ABSTRACT: A novel hierarchical structure of bimetal sulfide FeS_2@SnS_2 with the 1D/2D heterostructure was developed for high-performance sodium-ion batteries (SIBs). The FeS_2@SnS_2 was synthesized through a hydrothermal reaction and a sulphuration process. The exquisite 1D/2D heterostructure is featured with 2D SnS_2 nanoflakes anchoring on the 1D FeS_2 nanorod. This well-designed FeS_2@SnS_2 provides shortened ion diffusion pathway and adequate surface area, which facilitates the Na^+ transport and capacitive Na^+ storage. Besides, the FeS_2@SnS_2 integrates the 1D/2D synthetic structural advantages and synthetic hybrid active material. Consequently, the FeS_2@SnS_2 anode exhibits high initial specific capacity of 765.5 $mAh·g^{-1}$ at 1 $A·g^{-1}$ and outstanding reversibility (506.0 $mAh·g^{-1}$ at 1 $A·g^{-1}$ after 200 cycles, 262.5 $mAh·g^{-1}$ at 5 $A·g^{-1}$ after 1400 cycles). Moreover, the kinetic analysis reveals that the FeS_2@SnS_2 anode displays significant capacitive behavior which boosts the rate capacity.

KEYWORDS: sodium-ion battery; FeS_2@SnS_2; 1D/2D; capacitance behavior

Contents

Received December 14, 2021; accepted February 18, 2022

E-mail: luzhenxiao66@163.com

1 Introduction

The ever-expanding application of electric vehicle and large-scale energy storage system motivate the development of rechargeable batteries with high power/energy density and price competitiveness [1]. Lithium-ion batteries (LIBs) have been regarded as the most developed battery system used in electronic devices for recent ten years due to their enhanced electrochemical performance. However, the further wide utilization of LIBs and the limited resource on earth raise the price of lithium [2–3]. Sodium-ion batteries (SIBs) are promising alternatives because of the low cost of sodium and its similar physiochemical properties to lithium [4–5]. However, the developed anode materials for LIBs deliver poor cycle stability and low energy capacity in SIBs due to the larger diameter of Na^+. Therefore, the development of advancing SIBs lies in searching for suitable anode materials [6].

Among a wide range of materials which have been explored to date, metal sulfides are deemed as an advantageous class of SIB anode materials [7]. Generally, metal sulfides yield high theoretical capacity originating from the multi-electron transfer conversion and alloying reaction. In addition, metal sulfides exhibit better kinetic properties because of their weaker M−S bond, which results in better reversibility and higher first-cycle efficiency [8–12]. Among all of the metal sulfides, FeS_2 has attracted extensive investigations for its non-toxic nature and rich reserves [13]. Some researchers combine FeS_2 with carbonaceous materials to improve the conductivity and enhance the structural stability during the cycling process [14–16]. However, the carbon in the composite contributes fairly little capacity from the adsorption reaction with Na^+. Besides, adjusting cut-off voltage and using ether-based electrolyte were tried for single FeS_2 without carbon modification. The conversion reaction was successfully forbidden to avoid the large volume expansion, however, at the expense of capacity sacrifice [17]. Hence, the single FeS_2 cannot meet all the requirements as a high-performance electrode, and constructing nanocomposites with the hybrid structure is regarded to be capable of effectively reducing the ion-diffusion resistance and boosting the interfacial electron transport [18–20].

SnS_2 was reported to be an ideal material for hosting Na^+ ions for its layered microstructure and large interlayer spacing, which could boost the ion-diffusion efficiency and provide relatively large connect area with electrolyte [21–26]. However, the layered SnS_2 is easily overlapped due to its high surface energy. The direct use of single SnS_2 may lead to sever polarization and low utilization, and thus poor performance as the anode for SIBs. In order to leverage advantages of SnS_2 and realize its potential as the high-performance anode, combining carbon species with SnS_2 is a common practice, which is similar to the modification route of FeS_2 [26]. However, the relatively high carbon content results in low capacity and tapping density. Besides, graphene was also investigated to be mixed with SnS_2, but they tend to restacking during the cycling, which leads to poor cyclability [21–22]. The hybrid consisting of bi-component was reported to show improved sodium storage ability due to the synergistic effect of the two components [25]. Especially, properly assembled hierarchical nanohybrids with the advantageous structure will gather the intrinsic interactions of each component to obtain better electrochemical properties of SIBs. Based on these concepts, the hybrid with incorporated FeS_2 and SnS_2 may be promising to obtain high Na^+ storage performance.

In this work, we assembled a 1D/2D nanocomposite with 2D SnS_2 nanoflakes anchoring on the surface of the 1D FeS_2 core (FeS_2@SnS_2). This synthetic 1D/2D structure efficiently avoids the aggregation of SnS_2 nanoflakes and exploits the structural merits of both 1D FeS_2 nanorods and 2D SnS_2 nanoflakes. The FeS_2@SnS_2 possesses long-range lattice order and large specific surface area, which not only facilitate good charge-transfer dynamics, but also promote the Na^+ storage kinetics via capacitance behavior during the charge process [24–25]. Besides, both FeS_2 and SnS_2 possess high theoretical capacity based on the multistep electrochemical reaction [26]. As a result, the FeS_2@SnS_2 anode delivers a high initial specific capacity of 765.5 $mAh\cdot g^{-1}$ and a reversible capacity of 506.0 $mAh\cdot g^{-1}$ after 200 cycles at the current density of 1.0 $A\cdot g^{-1}$. This electrode also exhibits outstanding rate property with 262.5 $mAh\cdot g^{-1}$ at the current density of 5 $A\cdot g^{-1}$ after 1400 cycles.

2 Experimental

2.1 Preparation of nanorods

1) α-FeOOH nanorods: At first, 20 mL $Fe(NO_3)_3\cdot 9H_2O$ solution (0.05 $mol\cdot L^{-1}$) and 20 mL KOH solution (0.12 $mol\cdot L^{-1}$) were prepared and mixed together. After stirring for 30 min, the mixture was then transferred into a Teflon-lined stainless-steel autoclave. Subsequently, the autoclave was placed in an oven and heated at 100 °C for 24 h. At last, the product was washed and dried in an oven at 60 °C for 12 h.

2) α-FeOOH@SnO_2 nanorods: 0.1 g α-FeOOH was dispersed into 30 mL mixture containing H_2O and ethanol (with the volume ratio of 2:1). Then, 0.9 g urea and 0.144 g $K_2SnO_3\cdot H_2O$ were added into the solution and stirred for 30 min. Finally the solution was transferred into a Teflon-lined stainless-steel autoclave and heated at 170 °C for 1 h.

3) FeS_2@SnS_2 nanorods: 0.05 g α-FeOOH@SnO_2 and 1 g sulfur powder were placed in a porcelain boat and annealed in nitrogen atmosphere at 500 °C for 2 h with a heating rate of 2 $°C\cdot min^{-1}$.

2.2 Materials characterization

The component and crystallinity of as-synthesized products were demonstrated by X-ray diffraction (XRD) analysis (Bruker D8 diffractometer with Cu Kα radiation, λ = 0.15418 nm) and X-ray photoelectron spectroscopy (XPS; Axis Ultra DLD, Kratos Analytical). The morphologies were characterized via scanning electron microscopy (SEM; JSM-7600F). Thermogravimetric analysis (TGA) was conducted on a thermal analyzer apparatus (Mettler Toledo TGA/SDTA851) from 25 to 700 °C in air.

2.3 Electrochemical measurements

The $FeS_2@SnS_2$ electrode contains $FeS_2@SnS_2$ powder, acetylene black, and sodium carboxymethyl cellulose (CMC) with a weight ratio of 7:2:1. This mixture was fully porphyrized with added deionized water as the solvent. The formed slurry was pasted on Cu foils with uniform thickness. The Cu foils was dried in a vacuum oven at 60 °C for 12 h and punched into disks with the diameter of 12 mm. The mass loading of each electrode was about 1.5 $mg \cdot cm^{-2}$. The sodium-ion cells were assembled in a glove-box with high-purity argon as protective atmosphere. Metallic sodium with suitable size and thickness was used as the counter electrode. The $FeS_2@SnS_2$ electrode and the counter electrode were separated by the Whatman GF/F separator and soaked in the electrolyte of 1 $mol \cdot L^{-1}$ $NaPF_6$ in diethylene glycol dimethyl ether (DIGDME). The cycling performance of the cells was tested on a Land CT2001A battery tester with the cut-off voltage of 0.01–3 V. The cyclic voltammetry (CV) curves at different scan rates were collected on a CHI-760 electrochemical workstation.

3 Results and discussion

The procedures for the preparation of $FeS_2@SnS_2$ are displayed in Scheme 1(a). Firstly, α-FeOOH nanorods were prepared and served as the template. Then, SnO_2 nanocrystals were grown on the surface of α-FeOOH nanorods through a hydrothermal reaction to form core–shell α-$FeOOH@SnO_2$ nanorods [27]. Finally, the α-FeOOH@SnO_2 nanorods were sulfurized at 500 °C under N_2 atmosphere to obtain the $FeS_2@SnS_2$ composite. In such a comprehensive structure, the heterointerface could promote the e^-/Na^+ transportation and accelerate the charge transfer kinetic (Scheme 1(b)). Moreover, different redox potentials of FeS_2 and SnS_2 would contribute to smooth volume expansion and structural stability during the sodiation process [24–25]. The 2D SnS_2 nanoflakes (Scheme 1(c)) provide the shortened ion diffusion pathway and sufficient connect area with the electrolyte, which facilitates the capacitance behavior and improves the rate property.

The sample composition was characterized by the XRD measurement. As shown in Fig. 1(a), there are peaks indexed to FeS_2 (JCPDS No. 42-1340) and SnS_2 (JCPDS No. 23-0677) [28–29], and no SnO_2 phase can be found, demonstrating that all SnO_2 particles were transformed into SnS_2 through the sulphuration process. The TGA thermograms of $FeS_2@SnS_2$ and neat FeS_2 are displayed in Fig. 1(b). The weight losses of FeS_2 and $FeS_2@SnS_2$ are almost simultaneous. For $FeS_2@SnS_2$, the weight loss before 200 °C is due to the evaporation of water adsorbed on the sample surface. The mass loss occurring during 320–388 °C is related to the transformation of FeS_2 to FeS and $Fe_2(SO_2)_3$. The weight loss at 620 °C is attributed to the formation of Fe_2O_3 and SnO_2. For FeS_2, the weight loss at 620 °C is attributed to the formation of Fe_2O_3. The total weight loss ratio of FeS_2 is about 31.3%, which is close to the theoretical value of 33.3%. The total weight loss of $FeS_2@SnS_2$ is 24%, and thus, the content of FeS_2 in the composite can be calculated to be 43.8% [30].

To further analyze elemental compositions and valence states of the $FeS_2@SnS_2$ composite, XPS was carried out. Figure 1(c) shows the survey spectrum of $FeS_2@SnS_2$, which contains distinguishable peaks of Fe, Sn, S, and O. The O peak is due to the oxidation of the sample by O_2 in air. The Fe 2p spectrum (Fig. 1(d)) can be divided into two

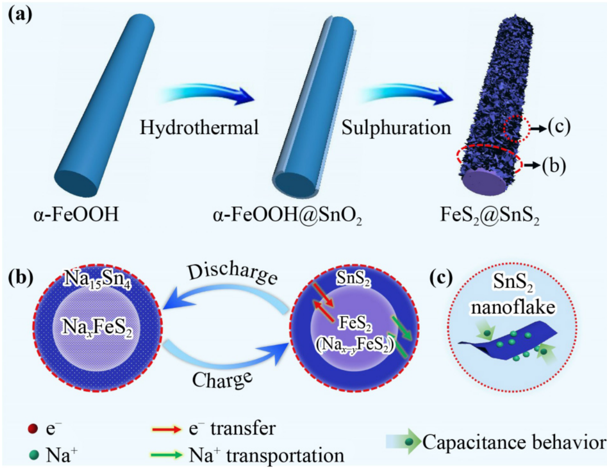

Scheme 1 Systematic illustrations of (**a**) the preparation process of $FeS_2@SnS_2$, (**b**) the electrochemical transformation during the charging/discharging process, and (**c**) the enlargement of the SnS_2 nanoflake.

peaks at 707.5 and 720.3 eV, corresponding to Fe $2p_{3/2}$ and Fe $2p_{1/2}$, respectively [30]. As shown in Fig. 1(d), there is no Fe–Sn peak that can be found in the XPS spectra, which illustrates that the combination mode of FeS_2 and SnS_2 is intermolecular binding. The Sn 3d spectrum (Fig. 1(e)) shows two peaks at 486.5 eV (Sn $3d_{5/2}$) and 494.9 eV (Sn $3d_{3/2}$) [19]. The XPS spectrum of S 2p (Fig. 1(f)) contains two peaks located at 162.3 and 163.3 eV, which consist of binding energies of S $2p_{3/2}$ and S $2p_{1/2}$, respectively [19].

Morphological features of the precursor and the FeS_2@SnS_2 composite were characterized by SEM and transmission electron microscopy (TEM). Figures 2(a) and 2(b) display that the SnO_2 nanoparticles were anchored uniformly on the outer-surface of α-FeOOH nanorods. After the sulphuration process, the 1D core retained (Figs. 2(c) and 2(d)), while the SnO_2 nanoparticles were transformed into SnS_2 nanoflakes with the irregular shape (Fig. 2(e)). To further investigate the crystalline of nanoflakes, high-resolution transmission electron microscopy (HRTEM) was carried out. Figure 2(f) reveals clear lattice fringes, where the lattice distances of 0.27 and 0.31 nm are indexed to (1 0 1) and (1 0 0) planes of SnS_2, respectively [31–32].

Figure 3(a) shows charge/discharge profiles of the FeS_2@SnS_2 electrode at a current density of 1 $A\cdot g^{-1}$. In

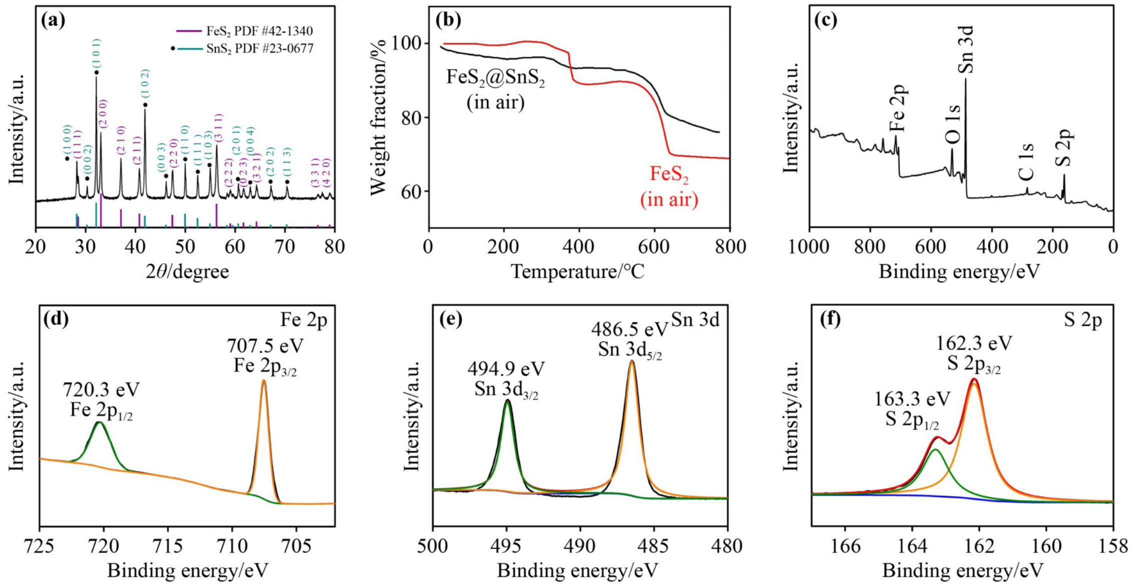

Fig. 1 (**a**) XRD pattern of FeS_2@SnS_2, (**b**) TGA curves of FeS_2@SnS_2 and neat FeS_2, and (**c**)(**d**)(**e**)(**f**) survey, Fe 2p, Sn 3d and S 2p XPS spectra of FeS_2@SnS_2.

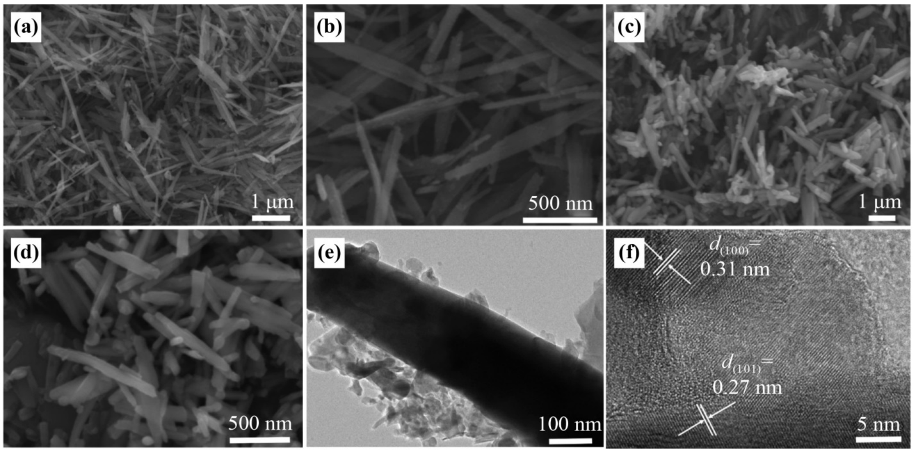

Fig. 2 (**a**) Low- and (**b**) high-resolution SEM images of α-FeOOH@SnO_2. (**c**) Low- and (**d**) high-resolution SEM images of FeS_2@SnS_2. (**e**) TEM image of FeS_2@SnS_2. (**f**) HRTEM image of the SnS_2 nanoflake.

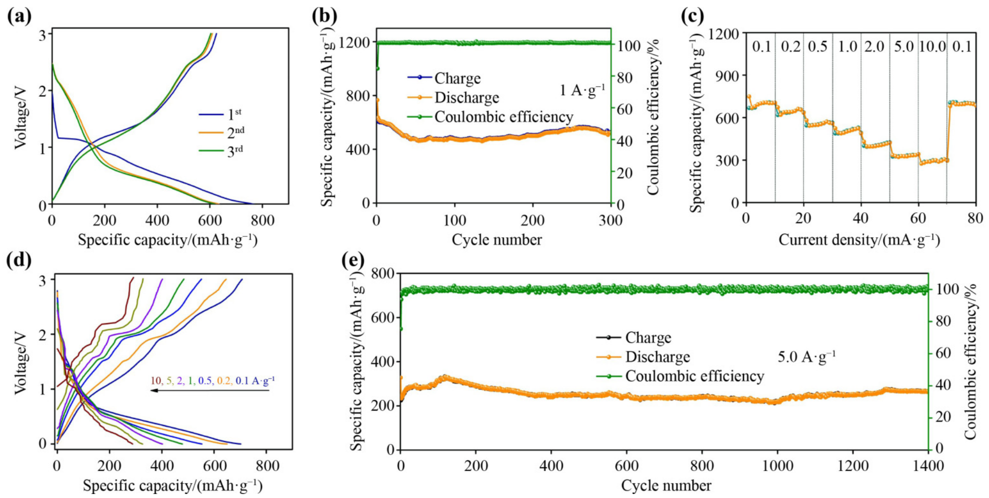

Fig. 3 Electrochemical properties of the FeS_2@SnS_2 electrode in SIBs: (**a**) charge/discharge profiles at 1 $A \cdot g^{-1}$, (**b**) cycling performance at 1 $A \cdot g^{-1}$, (**c**) rate property, (**d**) charge/discharge profiles at various current densities, and (**e**) cycling performance at 5 $A \cdot g^{-1}$.

the first cycle, the FeS_2@SnS_2 electrode delivers an initial discharge capacity of 765.5 $mAh \cdot g^{-1}$ and a charge capacity of 625.2 $mAh \cdot g^{-1}$, affording a coulombic efficiency of 81.6%. The irreversible capacity loss can be attributed to the decomposition of the electrode and the formation of the solid electrolyte interface (SEI) film [33]. In the second cycle, a discharge capacity of 635.2 $mAh \cdot g^{-1}$ and a charge capacity of 609.7 $mAh \cdot g^{-1}$ are achieved by the FeS_2@SnS_2 electrode, which correspond to a coulombic efficiency of 95.9%. The superior high specific capacity derived from the multi-electron transfer conversion and alloying reaction of FeS_2 and SnS_2 [11]. Figure 3(b) demonstrates the cycling performance of the FeS_2@SnS_2 electrode at the current density of 1 $A \cdot g^{-1}$. The capacity decay in the first 30 cycles is due to the formation of the SEI film, which is common in other metal chalcogenides [33]. Finally, the specific capacity tends to be stable and retains at 506.0 $mAh \cdot g^{-1}$ after 200 cycles.

The rate property of the FeS_2@SnS_2 electrode at various current densities is displayed in Fig. 3(c). At current densities of 0.1, 0.2, 0.5, 1.0, 2.0, 5.0, and 10.0 $A \cdot g^{-1}$, the specific capacities of the FeS_2@SnS_2 electrode are 705.5, 641.3, 553.2, 506.7, 402.2, 326.1, and 288.1 $mAh \cdot g^{-1}$, respectively. More importantly, when the current density switches to 0.1 $A \cdot g^{-1}$, the specific capacity returns to the beginning level of 705.1 $mAh \cdot g^{-1}$, indicating the outstanding reversibility of the FeS_2@SnS_2 electrode. The rate property is also demonstrated via charge/discharge profiles at different current densities ranging from 0.1 to 10 $A \cdot g^{-1}$ as shown in Fig. 3(d). The profiles yield distinct plateaus even at high current densities, illustrating the outstanding rate performance and slight polarization [34]. Besides, the FeS_2@SnS_2 electrode also exhibits superior rate performance compared with similar electrode materials (Fig. S1) [22,28,30–34]. In Fig. 3(e), the FeS_2@SnS_2 electrode exhibits an excellent reversible capacity of 262.5 $mAh \cdot g^{-1}$ after 1400 cycles at a high current density of 5 $A \cdot g^{-1}$. As detected, the capacity increases to 314 $mAh \cdot g^{-1}$ gradually before the 150th cycle, and then decays slowly. This phenomenon is caused by the improved Na^+ diffusion kinetics stemming from the activation of the electrode material and the stabilization of the repeated Na^+ insertions/extractions process [35–36]. Overall, the above mentioned superior cycling performance of FeS_2@SnS_2 is associated with the 1D/2D structure, which facilitates the ion diffusion and enlarges the connect area with the electrolyte. Another helpful factor is the synergistic interaction between FeS_2 and SnS_2, which derives from the heterogeneous structure and discrepant-electrochemical reactions [25]. Furthermore, the capacitive behavior may also conduce to the high performance of FeS_2@SnS_2.

Figure 4(a) shows CV curves of initial three cycles. In the first discharge process, the broad peak around 1.76 V and the distinct peak at 1.2 V indicate the insertion of Na^+ into SnS_2 and FeS_2 (Eqs. (1) and (2)) [28,37]:

$$SnS_2 + Na^+ + e^- \rightarrow NaSnS_2 \tag{1}$$

$$FeS_2 + xNa^+ + xe^- \rightarrow Na_xFeS_2 \ (x < 2) \tag{2}$$

The peak at 1.2 V disappears in the subsequent cycles.

Subsequently, a series of peaks appear at 0.8–0.4 V, which demonstrate the further insertion of Na^+ into Na_xFeS_2 (Eq. (3)), the conversion reaction between Na^+ and $NaSnS_2$ (Eqs. (4) and (5)), the alloying reaction (Eq. (6)) and the formation of the SEI film [38–40]:

$$Na_xFeS_2 + (4-x)Na^+ + (4-x)e^- \leftrightarrow Fe + 2Na_2S \tag{3}$$

$$NaSnS_2 + Na^+ + e^- \leftrightarrow SnS + Na_2S \tag{4}$$

$$SnS + 2Na^+ + 2e^- \leftrightarrow Sn + Na_2S \tag{5}$$

$$4Sn + 15Na^+ + 15e^- \leftrightarrow Na_{15}Sn_4 \tag{6}$$

In the following charging process, anodic peaks located at 0.24 and 1.24 V reveal the dealloying process (reverse of Eq. (6)), the restitution of SnS_2 (reverse of Eqs. (5), (4) and (1)) and the formation of Na_xFeS_2 (reverse of Eq. (3)) [27,37–40]. In the subsequent cycles, the anodic peak at 2.5 V and the cathodic peak at 2.1 V in the subsequent discharging process correspond to the reversible reaction (Eq. (7)) [6]:

$$Na_xFeS_2 \leftrightarrow Na_{x-y}FeS_2 + yNa^+ + ye^- \ (0 < y < x) \tag{7}$$

Obviously, the two components in the FeS_2@SnS_2 hybrid undergo asynchronous electrochemical reactions during the cycling, which would efficiently relieve the volume change and contribute to the stable cyclicity [25].

The kinetic analysis of FeS_2@SnS_2 nanorods was carried out to further analyze the excellent rate performance and cycle stability via CV curves at various scan rates. In Fig. 4(b), the CV curves of FeS_2@SnS_2/Na batteries at various scan rates share a similar shape, all including distinct cathodic and anodic peaks. Generally, the relationship between the peak current (i) and the scan rate (v) follows Eq. (8) [41–42]:

$$i = av^b \tag{8}$$

where both a and b are constants. Generally, b = 0.5 represents the diffusion process dominating the storage, and b = 1.0 demonstrates the capacitance process dominating the storage [43]. The b values corresponding to each peak can be calculated based on the transformation of Eq. (8) as follows:

$$\lg i = b \lg v + a \tag{9}$$

The b value is calculated to be between 0.68 and 0.98 (Fig. 4(c)), illustrating that both the diffusion-controlled and the capacitive processes dominate the charge process [43]. In other words, the capacitance behavior contributes to the total Na^+ storage. According to Eq. (10), the current at a fixed voltage $i(V)$ originates from both the diffusion-controlled process ($k_2v^{1/2}$) and the capacitive process (k_1v), where k_1 and k_2 are parameters at a given potential

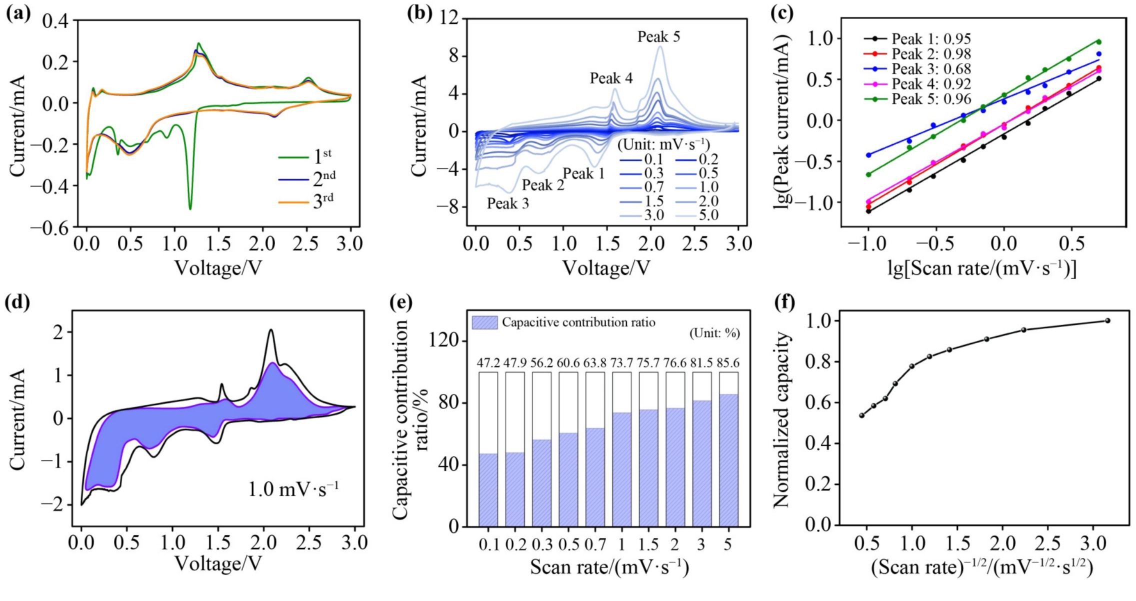

Fig. 4 FeS_2@SnS_2/Na batteries: (**a**) CV curves for the initial three cycles at the scan rate of 0.1 $mV \cdot s^{-1}$; (**b**) CV curves at different scan rates; (**c**) b values of different peaks in panel (b); (**d**) CV curve with the capacitance controlled current shown by the shaded section; (**e**) contribution ratios of the capacitive storage to the total capacity at different scan rates; (**f**) variation of the normalized capacity with $v^{-1/2}$ (v is the scan rate).

[44]. Then, the contribution ration of the capacitive Na^+ storage process can be quantitatively determined based on Eq. (10):

$$i(V) = k_1 v + k_2 v^{1/2} \tag{10}$$

Current originating from the capacitive storage is shown in Fig. 4(d), and the shaded area demonstrates the capacitive contribution to the total capacity (the area of the CV curve). Similarly, the capacitive contribution at various scan rates can be evaluated. The capacitive Na^+ storage ratio gradually increases as the scan rate raises (Fig. 4(e)), which illustrates that the capacitive mechanism dominates the storage capability, especially at high rates [17,28]. At the scan rate of 5 $mV\cdot s^{-1}$, 85% of the total capacity comes from the capacitive Na^+ storage mechanism, accounting for the high rate property of FeS_2@SnS_2. Besides, the relationship between the normalized capacity and the scan rate is shown in Fig. 4(f) to distinguish the storage mechanism. For $v > 1.0$ $mV\cdot s^{-1}$, the capacity decreases as the scan rate increases, indicating that the diffusion-controlled process is limited at high rates. For 0.1 $mV\cdot s^{-1} < v <$ 1.0 $mV\cdot s^{-1}$, the capacity does not decrease significantly as the scan rate rises, reflecting that the capacitive process is independent of the scan rate [6,44]. This significant capacitive behavior benefits from the favorable structure with the sufficient surface area, which is vital for the capacitive Na^+ storage [17].

4 Conclusions

In summary, the FeS_2@SnS_2 composite featured with SnS_2 nanoflakes adhering to 1D FeS_2 core was prepared and its excellent electrochemical performance as the anode for SIBs was explored. Benefiting from the hybrid structure and the bicomponent active material, the FeS_2@SnS_2 anode delivered a reversible capacity of 506.0 $mAh\cdot g^{-1}$ after 200 cycles at 1 $A\cdot g^{-1}$. Moreover, FeS_2@SnS_2 achieved excellent long-term cyclability of 262.5 $mAh\cdot g^{-1}$ after 1400 cycles at 5 $A\cdot g^{-1}$. Such high rate performance was further investigated and confirmed to be associated with the capacitive storage mechanism, which contributes considerable capacity. These results indicate that the FeS_2@SnS_2 composite is a promising anode for SIBs with high-rate capability and long cycle life. This hybrid material provides an example for a series of multicomponent hybrid electrodes which may be applied in batteries.

Acknowledgements This work was financially supported by the National Natural Science Foundation of China (Grant Nos. 21501101 and 52004100), the Natural Science Foundation of Henan Province (Grant No. 182300410226), and Nanyang Normal University (Grant No. 2022ZX007).

References

[1] Ma Y J, Ma Y, Giuli G, et al. Introducing highly redox-active atomic centers into insertion-type electrodes for lithium-ion batteries. Advanced Energy Materials, 2020, 10(25): 2000783

[2] Ku K, Kim B, Jung S K, et al. A new lithium diffusion model in layered oxides based on asymmetric but reversible transition metal migration. Energy & Environmental Science, 2020, 13(4): 1269–1278

[3] Jia Y, Ma Z, Li Z, et al. Electrochemical performances of NiO/Ni_2N nanocomposite thin film as anode material for lithium ion batteries. Frontiers of Materials Science, 2019, 13(4): 367–374

[4] Wu X, Xu Y, Zhang C, et al. Reverse dual-ion battery via a $ZnCl_2$ water-in-salt electrolyte. Journal of the American Chemical Society, 2019, 141(15): 6338–6344

[5] Zhang Y, Tao L, Xie C, et al. Defect engineering on electrode materials for rechargeable batteries. Advanced Materials, 2020, 32(7): 1905923

[6] Lu Z X, Zhai Y J, Wang N N, et al. FeS_2 nanoparticles embedded in N/S co-doped porous carbon fibers as anode for sodium-ion batteries. Chemical Engineering Journal, 2020, 380: 122455

[7] Yang C, Xin S, Mai L, et al. Materials design for high-safety sodium-ion battery. Advanced Energy Materials, 2021, 11(2): 2000974

[8] Xu X, Lin K, Zhou D, et al. Quasi-solid-state dual-ion sodium metal batteries for low-cost energy storage. Chem, 2020, 6(4): 902–918

[9] Liu P, Han J, Zhu K, et al. Heterostructure $SnSe_2$/ZnSe@PDA nanobox for stable and highly efficient sodium-ion storage. Advanced Energy Materials, 2020, 10(24): 2000741

[10] Lu X, Luo J, Matios E, et al. Enabling high-performance sodium metal anodes via a sodiophilic structure constructed by hierarchical Sb_2MoO_6 microspheres. Nano Energy, 2020, 69: 104446

[11] Zhai H, Jiang H, Qian Y, et al. Sb_2S_3 nanocrystals embedded in multichannel N-doped carbon nanofiber for ultralong cycle life sodium-ion batteries. Materials Chemistry and Physics, 2020, 240: 122139

[12] Chen W Y, Jiang X, Lai S N, et al. Nanohybrids of a MXene and transition metal dichalcogenide for selective detection of volatile organic compounds. Nature Communications, 2020, 11(1): 1302

[13] Wang F B, Li G D, Cui W F. FeS_2 hollow nanospheres as high-performance anode for sodium ion battery and their surface pseudocapacitive properties. Journal of Nanoparticle Research, 2019, 21(6): 121

[14] Lin Z, Xiong X, Fan M, et al. Scalable synthesis of FeS_2 nanoparticles encapsulated into N-doped carbon nanosheets as a high-performance sodium-ion battery anode. Nanoscale, 2019, 11(9): 3773–3779

[15] Wang S W, Jing Y P, Han L F, et al. Ultrathin carbon-coated FeS_2 nanooctahedra for sodium storage with long cycling stability. Inorganic Chemistry Frontiers, 2019, 6(2): 459–464

[16] Zang R, Li P X, Guo X, et al. Yolk–shell N-doped carbon coated FeS_2 nanocages as a high-performance anode for sodium-ion batteries. Journal of Materials Chemistry A: Materials for Energy and Sustainability, 2019, 7(23): 14051–14059

[17] Cao L, Gao X, Zhang B, et al. Bimetallic sulfide Sb_2S_3@FeS_2 hollow nanorods as high-performance anode materials for sodium-ion batteries. ACS Nano, 2020, 14(3): 3610–3620

[18] Luo B, Hu Y X, Zhu X B, et al. Controllable growth of SnS_2 nanostructures on nanocarbon surfaces for lithium-ion and sodium-ion storage with high rate capability. Journal of Materials Chemistry A: Materials for Energy and Sustainability, 2018, 6(4): 1462–1472

[19] Wu Y T, Nie P, Wu L Y, et al. 2D MXene/SnS_2 composites as high-performance anodes for sodium ion batteries. Chemical Engineering Journal, 2018, 334: 932–938

[20] Wang S, Liu S, Li X, et al. SnS_2/Sb_2S_3 heterostructures anchored on reduced graphene oxide nanosheets with superior rate capability for sodium-ion batteries. Chemistry, 2018, 24(15): 3873–3881

[21] Zhang X, Zhou J, Zheng Y, et al. $Co_{0.85}Se$ nanoparticles encapsulated by nitrogen-enriched hierarchically porous carbon for high-performance lithium-ion batteries. ACS Applied Materials & Interfaces, 2020, 12(8): 9236–9247

[22] Xia J, Jiang K, Xie J, et al. Tin disulfide embedded in N-, S-doped carbon nanofibers as anode material for sodium-ion batteries. Chemical Engineering Journal, 2019, 359: 1244–1251

[23] Ma M, Zhang S, Yao Y, et al. Heterostructures of 2D molybdenum dichalcogenide on 2D nitrogen-doped carbon: superior potassium-ion storage and insight into potassium storage mechanism. Advanced Materials, 2020, 32(22): 2000958

[24] Zhao Y, Wang F, Wang C, et al. Encapsulating highly crystallized mesoporous Fe_3O_4 in hollow N-doped carbon nanospheres for high-capacity long-life sodium-ion batteries. Nano Energy, 2019, 56: 426–433

[25] Yang C, Liang X, Ou X, et al. Heterostructured nanocube-shaped binary sulfide $(SnCo)S_2$ interlaced with S-doped graphene as a high-performance anode for advanced Na^+ batteries. Advanced Functional Materials, 2019, 29(9): 1807971

[26] Ren X C, Wang J S, Zhu D M, et al. Sn−C bonding riveted SnSe nanoplates vertically grown on nitrogen-doped carbon nanobelts for high-performance sodium-ion battery anodes. Nano Energy, 2018, 54: 322–330

[27] Liu Y H, Yu X Y, Fang Y J, et al. Confining SnS_2 ultrathin nanosheets in hollow carbon nanostructures for efficient capacitive sodium storage. Joule, 2018, 2(4): 725–735

[28] Zhao Y, Wang J J, Ma C L, et al. Interconnected graphene nanosheets with confined FeS_2/FeS binary nanoparticles as anode material of sodium-ion batteries. Chemical Engineering Journal, 2019, 378: 122168

[29] Liu Y, Kang H, Jiao L, et al. Exfoliated-SnS_2 restacked on graphene as a high-capacity, high-rate, and long-cycle life anode for sodium ion batteries. Nanoscale, 2015, 7(4): 1325–1332

[30] Chen C M, Yang Y C, Tang X, et al. Graphene-encapsulated FeS_2 in carbon fibers as high reversible anodes for Na^+/K^+ batteries in a wide temperature range. Small, 2019, 15(10): 1804740

[31] Zeng L, Zhang L P, Liu X G, et al. SnS_2 nanocrystalline-anchored three-dimensional graphene for sodium batteries with improved rate performance. Nanomaterials, 2020, 10(12): 2336

[32] Li Y F, Wang S G, Shi Y H, et al. *In situ* chemically encapsulated and controlled SnS_2 nanocrystal composites for durable lithium/sodium-ion batteries. Dalton Transactions, 2020, 49(44): 15874–15882

[33] Shao M, Cheng Y, Zhang T, et al. Designing MOFs-derived FeS_2@carbon composites for high-rate sodium ion storage with capacitive contributions. ACS Applied Materials & Interfaces, 2018, 10(39): 33097–33104

[34] Wang S W, Jing Y P, Han L F, et al. Ultrathin carbon-coated FeS_2 nanooctahedra for sodium storage with long cycling stability. Inorganic Chemistry Frontiers, 2019, 6(2): 459–464

[35] Liu Y, Hu X, Zhong G, et al. Layer-by-layer stacked nanohybrids of N,S-co-doped carbon film modified atomic MoS_2 nanosheets for advanced sodium dual-ion batteries. Journal of Materials Chemistry A: Materials for Energy and Sustainability, 2019, 7(42): 24271–24280

[36] Ren X, Zhu Y, Li Q, et al. A novel multielement nanocomposite with ultrahigh rate capacity and durable performance for sodium-ion battery anodes. Journal of Materials Chemistry A: Materials for Energy and Sustainability, 2020, 8(23): 11598–11606

[37] Gao P, Zhang Y Y, Wang L P, et al. *In situ* atomic-scale observation of reversible sodium ions migration in layered metal dichalcogenide SnS_2 nanostructures. Nano Energy, 2017, 32: 302–309

[38] Li J, Han L, Li Y, et al. MXene-decorated SnS_2/Sn_3S_4 hybrid as anode material for high-rate lithium-ion batteries. Chemical

Engineering Journal, 2020, 380: 122590

[39] Cao L, Zhang B, Ou X, et al. Synergistical coupling interconnected ZnS/SnS_2 nanoboxes with polypyrrole-derived N/S dual-doped carbon for boosting high-performance sodium storage. Small, 2019, 15(9): 1804861

[40] Zhao J, Yu X, Gao Z G, et al. One step synthesis of SnS_2 nanosheets assembled hierarchical tubular structures using metal chelate nanowires as a soluble template for improved Na-ion storage. Chemical Engineering Journal, 2018, 332: 548–555

[41] Xue P, Wang N, Fang Z, et al. Rayleigh-instability-induced bismuth nanorod@nitrogen-doped carbon nanotubes as a long cycling and high rate anode for sodium-ion batteries. Nano Letters, 2019, 19(3): 1998–2004

[42] Xu X, Zhao R S, Chen B, et al. Progressively exposing active facets of 2D nanosheets toward enhanced pseudocapacitive response and high-rate sodium storage. Advanced Materials, 2019, 31(17): 1900526

[43] Liu Y L, Wang N N, Zhao X H, et al. Hierarchical nanoarchitectured hybrid electrodes based on ultrathin $MoSe_2$ nanosheets on 3D ordered macroporous carbon frameworks for high-performance sodium-ion batteries. Journal of Materials Chemistry A: Materials for Energy and Sustainability, 2020, 8(5): 2843–2850

[44] Wang N, Wang Y, Xu X, et al. Defect sites-rich porous carbon with pseudocapacitive behaviors as an ultrafast and long-term cycling anode for sodium-ion batteries. ACS Applied Materials & Interfaces, 2018, 10(11): 9353–9361

Supplementary information

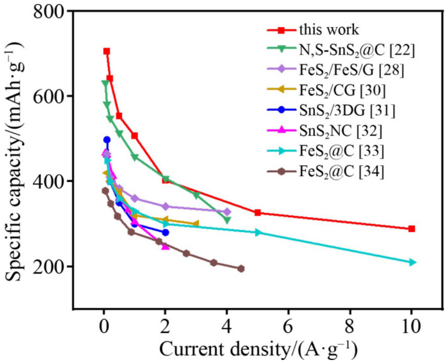

Fig. S1 A comprehensive comparison of the rate performance between this work and other related sulfide electrodes of SIBs.